The Cryosphere Discuss., 4, 1277–1306, 2010
www.the-cryosphere-discuss.net/4/1277/2010/
doi:10.5194/tcd-4-1277-2010


The Cryosphere Discussions



# The Potsdam Parallel Ice Sheet Model (PISM-PIK) – Part 1: Model description

**R. Winkelmann[1,2], M. A. Martin[1,2], M. Haseloff[1,3], T. Albrecht[1,2], E. Bueler[4], C. Khroulev[5], and A. Levermann[1,2]**

[1]Earth System Analysis, Potsdam Institute for Climate Impact Research, Potsdam, Germany
[2]Institute of Physics, Potsdam University, Potsdam, Germany
[3]Dept. of Physics, Humboldt-University, Berlin, Germany
[4]Dept. of Mathematics and Statistics, University of Alaska, Fairbanks, USA
[5]Geophysical Institute, University of Alaska, Fairbanks, USA

Received: 15 July 2010 – Accepted: 18 July 2010 – Published: 18 August 2010

Correspondence to: A. Levermann (anders.levermann@pik-potsdam.de)

Published by Copernicus Publications on behalf of the European Geosciences Union.







## Abstract

We present the Potsdam Parallel Ice Sheet Model (PISM-PIK), developed at the Potsdam Institute for Climate Impact Research to be used for simulations of large-scale ice sheet-shelf systems. It is derived from the Parallel Ice Sheet Model (Bueler and Brown, 2009). Velocities are calculated by superposition of two shallow stress balance approximations within the entire ice covered region: the shallow ice approximation (SIA) is dominant in grounded regions and accounts for shear deformation parallel to the geoid. The plug-flow type shallow shelf approximation (SSA) dominates the velocity field in ice shelf regions and serves as a basal sliding velocity in grounded regions. Ice streams naturally emerge through this approach and can be identified diagnostically as regions with a significant contribution of membrane stresses to the local momentum balance. All lateral boundaries in PISM-PIK are free to evolve, including the grounding line and ice fronts. Ice shelf margins in particular are modeled using Neumann boundary conditions for the SSA equations, reflecting a hydrostatic stress imbalance along the vertical calving face. The ice front position is modeled using a subgrid scale representation of calving front motion (Albrecht et al., 2010) and a physically motivated dynamic calving law based on horizontal spreading rates. The model is validated within the Marine Ice Sheet Model Intercomparison Project (MISMIP) and is used for a dynamic equilibrium simulation of Antarctica under present-day conditions in the second part of this paper (Martin et al., 2010).

## 1 Introduction

In order to understand the evolution of ice sheets, especially with respect to their contribution to sea-level rise, there is a need for numerical models which are able to capture the dynamics of sheet-shelf systems as a whole. To this end, there are various types of approaches: while one-dimensional "flowline" models are both computationally efficient and at the same time very useful for understanding basic processes (e.g., Dupont





TCD
4, 1277–1306, 2010



and Alley, 2005), they fail in answering questions regarding the role of ice shelves on the ice flow across the grounding line which is relevant for global sea level rise. Models which solve the complete Stokes stress balance (e.g., Martín et al., 2004; Jarosch and Gudmundsson, 2007; Pattyn, 2008), on the other hand, can not be used for large-scale, long-term, high resolution modeling because they are computationally too demanding. The same constraint substantially applies to intermediate, so-called higher order models (e.g., Blatter, 1995; Pattyn, 2003).

Models based on the Shallow Ice Approximation (Hutter, 1983) and the Shallow Shelf Approximation (Morland, 1987; Weis et al., 1999), each recalled in Sect. 2, decrease these computational costs. They make use of a scaling analysis of the full Stokes problem, using the fact that ice thickness is small compared to relevant horizontal scales, to enable simulations of whole ice sheets.

Various SIA-based models (e.g., Greve, 1997b; Payne, 1999; Marshall et al., 2000) provide a good approximation for the flow of ice that is frozen to the bedrock, but the equations are not meant to describe fast sliding processes. Traditionally some sliding of grounded ice is incorporated into such SIA models by adding a sliding velocity at the base of the ice column which depends directly on the height and surface slope of that column, in an attempt to simulate regions of higher velocity such as ice streams. By contrast, the SSA has been used to simulate the faster flow on ice shelves which have no basal friction (e.g., MacAyeal et al., 1996). This SSA ice shelf model has been combined with the SIA for the grounded ice (e.g., Huybrechts, 1990; Ritz et al., 2001), but with a resulting abrupt change in flow type across the grounding line.

Models that smoothly combine the two shallow approximations across grounding lines are now possible, however. Besides the model in the current paper, Pollard and Deconto (2009) have modeled Antarctic ice sheet growth and collapse through the past five million years, combining both shallow approximations via a heuristic shear stress correction and an additional grounding line velocity correction based on the one-dimensional approach by Schoof (2007b).





TCD
4, 1277–1306, 2010



A major difficulty faced by all ice dynamics models is the large difference in flow regimes and speeds throughout sheets, streams and shelves. The Potsdam Parallel Ice Sheet Model (PISM-PIK), developed at the Potsdam Institute for Climate Impact Research (PIK) and presented in this paper, is a new model for marine ice sheets which aims to incorporate these regimes in a universal manner. PISM-PIK is based on the Parallel Ice Sheet Model (PISM; Bueler and Brown, 2009), which is a three-dimensional thermodynamically-coupled shallow model using a finite-difference discretization. These models are innovative in using the SSA as a sliding law for grounded ice, thereby avoiding discontinuities at the onset of sliding, and provide a framework for consistently modeling sheet-shelf systems. Ice streams are modeled by the SSA stress balance and a plastic till model for basal mechanics (Schoof, 2006a). In aiming at modeling the Antarctic ice sheet and shelves (Martin et al., 2010), PIK modifications to PISM have been made particularly with respect to the shelf dynamics. Ice shelves are especially important for an assessment of past and future sea level contributions of Antarctica because of their buttressing effect on the dynamics upstream of the grounding line (De Angelis and Skvarca, 2003; Bamber et al., 2007; Rott et al., 2007; Glasser and Scambos, 2008; Rignot et al., 2008; Goldberg et al., 2009).

In Sect. 2 we describe PISM-PIK with special focus on the modifications from PISM. Section 3 addresses validation within the MISMIP intercomparison. A summary is given in Sect. 4. The second part of the paper (Martin et al., 2010) discusses the performance of PISM-PIK under present-day boundary conditions on Antarctica.

## 2 Model description

Our description of the model proceeds from the underlying continuum model to the numerical schemes. The major characteristics of the continuum model are adopted from PISM (Sect. 2.1), but modifications include changes to the way sliding occurs (Sect. 2.2) and major changes in the treatment of different ice fronts, especially calving fronts of ice shelves (Sects. 2.3–2.6).





TCD
4, 1277–1306, 2010



Boundary data provided to PISM-PIK are bed elevation $b$, surface mass balance $M$, geothermal flux $G$ and ocean temperature $T_o$. In the mode described in Martin et al. (2010), the surface temperature distribution is a parameterized function of latitude and elevation, and the model is initialized with observed ice thickness data from Lythe et al. (2001) and Le Brocq et al. (2010). In each time step, the model is solved for velocity $\boldsymbol{v}$, basal melt rate $S$ and calving rate $C$. Each time step updates the prognostic variables, which are ice temperature $T$ and thickness $H$. Because the bed elevations $b$ are fixed in time, each update to the ice thickness implies an update to surface elevation $h$. (For the notation throughout this paper see Table 1.)

Each of the model equations is numerically discretized, using a finite difference approach on a rectangular grid. Exactly as described in Bueler and Brown (2009), the new model PISM-PIK runs in parallel using the Portable, Extensible Toolkit for Scientific computation (PETSc) for solving every discretized model equation, including the SSA. Time stepping is explicit and adaptive. Technically speaking, PISM-PIK is implemented as derived classes of the C++ code of the open-source Parallel Ice Sheet Model (PISM), version stable0.2 (Bueler et al., 2008).

### 2.1 Field equations and shallow approximations

For completeness we give a short review of the field equations used both in PISM and PISM-PIK. For more details see Bueler and Brown (2009) and Bueler et al. (2007).

The equation of *mass continuity* describing the evolution of the ice thickness

$$\partial_t H = M - S - \nabla \cdot \boldsymbol{Q} \tag{1}$$

can be derived from incompressibility $\partial_\mu v_\mu = 0$ and the kinematic equations at the surface and base of the ice. (Throughout this paper, the Einstein summation convention is used.) Here $\boldsymbol{Q}$ is the vertical integral of the horizontal velocity. The mass continuity equation is solved numerically in each time step for $H$. The vertical velocity $v_z$ within





TCD
4, 1277–1306, 2010



the ice

$$v_z(z) = -S + \boldsymbol{v}_\mathrm{b} \cdot \boldsymbol{\nabla} b - \int_\mathrm{b}^z \boldsymbol{\nabla} \cdot \boldsymbol{v} \, d\zeta \tag{2}$$

is also given by incompressibility.

The velocity field advects the temperature in the following shallow equation of *conservation of energy*, which includes vertical conduction and strain dissipation heating terms (Greve and Blatter, 2009, Eq. 5.105)

$$\rho_\mathrm{i} c_\mathrm{i} \left( \partial_t T + v_\mu \partial_\mu T \right) = k_\mathrm{i} \partial_z^2 T + \Sigma \, . \tag{3}$$

The strain heating term ($\Sigma$) is described further in Bueler and Brown (2009). Surface temperature $T_\mathrm{s}$ and the geothermal flux as well as pressure melting temperature in the case of ice shelves provide boundary conditions for this equation.

The *flow law* is given by

$$\dot{\epsilon}_{ij} \equiv \frac{1}{2} \left( \partial_{x_j} v_i + \partial_{x_i} v_j \right) = E A(T^*) \left( \sqrt{1/2 \tau_{ij} \tau_{ij}} \right)^{n-1} \tau_{ij} \tag{4}$$

with $n$=3 and ice softness $A(T^*)$ from Paterson and Budd (1982)

$$A(T^*) = \begin{cases} (3.61 \times 10^{-13}) e^{-6.0 \times 10^4 / (RT^*)} \, , & T^* \leq 263.15 \, \mathrm{K} \, , \\ (1.73 \times 10^{+3}) e^{-13.9 \times 10^4 / (RT^*)} \, , & T^* > 263.15 \, \mathrm{K} \, . \end{cases} \tag{5}$$

The flow law has an inverted form

$$\tau_{ij} = 2 \nu \dot{\epsilon}_{ij} \tag{6}$$

in which the *effective viscosity* $\nu$ depends on the effective strain rate and the temperature (Greve and Blatter, 2009).

The Stokes stress balance for a flow viscous fluid (Greve and Blatter, 2009, Sect. 5.1) is approximated using two limiting *shallow approximations*.





TCD
4, 1277–1306, 2010



First, in an ice shelf where there is zero traction at the base of the ice, the driving stress is exclusively balanced by membrane stresses (viscous deformation), and the resulting plug flow is captured by the SSA (Morland, 1987; Weis et al., 1999), see Fig. 1 (*ice shelf*). The SSA stress balance allows the velocity field (solution) to be influenced by distant ice and thus is necessarily non-local. The stress balance equations themselves are the $\tau_b$=0 forms of the following:

$$\frac{\partial}{\partial x}\left[2\bar{\nu}H\left(2\frac{\partial v_x}{\partial x}+\frac{\partial v_y}{\partial y}\right)\right]+\frac{\partial}{\partial y}\left[\bar{\nu}H\left(\frac{\partial v_x}{\partial y}+\frac{\partial v_y}{\partial x}\right)\right]+\tau_{b,x}=\rho_i g H\frac{\partial h}{\partial x}, \tag{7}$$

$$\frac{\partial}{\partial x}\left[\bar{\nu}H\left(\frac{\partial v_x}{\partial y}+\frac{\partial v_y}{\partial x}\right)\right]+\frac{\partial}{\partial y}\left[2\bar{\nu}H\left(\frac{\partial v_x}{\partial x}+2\frac{\partial v_y}{\partial y}\right)\right]+\tau_{b,y}=\rho_i g H\frac{\partial h}{\partial y}, \tag{8}$$

with

$$\bar{\nu}=\frac{\bar{B}}{2}(E_{SSA})^{-\frac{1}{n}}\left[\frac{1}{2}\dot{\epsilon}_{ij}\dot{\epsilon}_{ij}+\frac{1}{2}\dot{\epsilon}_{ii}^2\right]^{\frac{1-n}{2n}} \tag{9}$$

for the *vertically-averaged effective viscosity*. Here $\bar{B}$ is the vertically-averaged ice hardness, $\dot{\epsilon}_{ij}$ is the strain rate tensor and $E_{SSA}$ is an enhancement factor. The stress balance equations can be re-expressed in terms of a vertically-integrated stress tensor (Schoof, 2006b)

$$T_{ij}\equiv 2\bar{\nu}H\left(\dot{\epsilon}_{ij}+\dot{\epsilon}_{kk}\delta_{ij}\right). \tag{10}$$

This gives the SSA stress balance a very compact form which is equivalent to Eqs. (7) and (8) together:

$$\frac{\partial T_{ij}}{\partial x_j}+\tau_{b,i}=\rho_i g H\frac{\partial h}{\partial x_i}. \tag{11}$$

Second, the SIA (Morland and Johnson, 1980; Hutter, 1983) is valid for regions where bottom friction is high enough for vertical shearing to dominate over horizontal





TCD
4, 1277–1306, 2010



shear and longitudinal stresses. The corresponding velocities are given by

$$\boldsymbol{v}_{\mathrm{SIA}} = -2(\rho_{\mathrm{i}} g)^n |\nabla h|^{n-1} \left[ \int_{\mathrm{b}}^{z} E_{\mathrm{SIA}} A(T^*)(h-\zeta)^n d\zeta \right] \nabla h \,. \tag{12}$$

Following MacAyeal (1989), the shallow shelf approximation (SSA) is also used with an additional term for basal drag (see also Schoof, 2006a) for modeling the fast flow regime in ice streams (a plug flow, see Fig. 1; *ice stream*). Thus ice streams are conceptualized as dragging ice shelves. Specifically, Eqs. (7) and (8) are used with nonzero basal friction $\tau_{\mathrm{b}}$, which is calculated based on a model for plastic till (Schoof, 2006a)

$$\tau_{\mathrm{b},i} = -\tau_{\mathrm{c}} \frac{v_i}{\left(v_x^2 + v_y^2\right)^{1/2}} \,. \tag{13}$$

This basal model assumes the till supports applied stresses without deformation until these reach a yield stress $\tau_{\mathrm{c}}$. Division by zero is avoided by the addition of a small constant in the denominator (Bueler and Brown, 2009). Yield stress is given by the Mohr-Coulomb model for saturated till, with till cohesion $c_0$ set to zero (Paterson, 1994)

$$\tau_{\mathrm{c}} = c_0 + (\tan\phi)(\rho_{\mathrm{i}} g H - p_{\mathrm{w}}) \,. \tag{14}$$

## 2.2 Velocity combination and sliding

Sliding is traditionally incorporated by adding a basal velocity $\boldsymbol{v}_{\mathrm{b}}$ to obtain the overall ice velocity

$$\boldsymbol{v} = \boldsymbol{v}_{\mathrm{b}} + \boldsymbol{v}_{\mathrm{SIA}} \,. \tag{15}$$

If $\boldsymbol{v}_{\mathrm{b}}$ were to depend directly and locally on the driving stress $\tau_{\mathrm{d},i} = \rho_{\mathrm{i}} g H \partial h / \partial x_i$ which enters expression (12) for $\boldsymbol{v}_{\mathrm{SIA}}$, then unbounded vertical velocities would arise





TCD
4, 1277–1306, 2010



from (physically-possible) abrupt changes in basal strength (Fowler, 2001; Bueler and Brown, 2009). In order to obtain a smooth transition from regions where the driving stress is fully balanced by vertical shearing (see Fig. 1; *ice sheet*) and those with significant sliding, a different approach is used, following the basic idea of superposition, or "SSA-as-a-sliding-law" (Bueler and Brown, 2009). Thus in PISM-PIK the basal velocities for grounded ice *are* the SSA velocities $\boldsymbol{v}_{\mathrm{SSA}} = \boldsymbol{v}_{\mathrm{b}}$. Through the superposition of the two velocity fields, each of which are differentiable, unbounded vertical velocities cannot arise.

In contrast to Bueler and Brown (2009, Eqs. 21 and 22), we do not use a weighting function for combining the SIA and SSA velocities, but simply superpose the contributions resulting from the two approximations. Schoof and Hindmarsh (2010) show that this combination of velocities, and hence of two shallow approximations, indeed yields a good shallow approximation of the full Stokes problem in the transition zone between ice sheet and ice shelf.

Hereby, qualitatively-different flow regimes with dominant vertical shearing on the ice sheet and dominant plug flow in ice streams naturally emerge, see Fig. 1. We diagnose an ice stream as a region where SSA velocities in the model output are larger than the total column contribution from SIA velocities

$$\boldsymbol{v}_{\mathrm{b}} > \bar{\boldsymbol{v}} - \boldsymbol{v}_{\mathrm{b}} \tag{16}$$

with $\bar{\boldsymbol{v}}$ the vertically averaged overall velocity. This definition is purely diagnostic and different physics for grounded ice is not prescribed according to this flow regime diagnosis.

The SIA contribution is taken into account on the whole sheet-shelf system, but experiments with simplified setups have shown that its contribution is negligible on shelves due to the low surface gradient. Hence the velocity and dynamics of shelves are determined by the SSA only.





TCD
4, 1277–1306, 2010



### 2.3 Calving front stress boundary condition

At the calving front, the imbalance between vertically-integrated stresses in the ice and the hydrostatic pressure exerted by the ocean contributes to the ice flow upstream of the calving front. A calving front stress boundary condition is necessary for solving the non-local SSA momentum balance Eqs. (7) and (8). It is also necessary for the application of a dynamic calving law (see Sect. 2.6) as a boundary condition to the mass continuity equation. PISM-PIK therefore incorporates a physical stress boundary condition (Weertman, 1957; Morland and Zainuddin, 1987) describing the stress imbalance at the calving front. By contrast, in PISM itself there is no such condition, and instead a notional ice shelf extends across the ice-free ocean to the edge of the computational domain. The effect of this extension, and the choice of its strength, are inadequately understood (MacAyeal et al., 1996; Bueler and Brown, 2009). The stress boundary condition implemented in PISM-PIK reads

$$\int_{z_{\mathrm{sl}}-\frac{\rho_\mathrm{i}}{\rho_\mathrm{o}}H_\mathrm{c}}^{z_{\mathrm{sl}}+\left(1-\frac{\rho_\mathrm{i}}{\rho_\mathrm{o}}\right)H_\mathrm{c}} \sigma_{\mu\nu}\cdot n_\nu \, dz = \frac{1}{2}\rho_\mathrm{o} g \left(\frac{\rho_\mathrm{i}}{\rho_\mathrm{o}}H_\mathrm{c}\right)^2 n_i \, . \tag{17}$$

The deviatoric part of the left hand side can be expressed in terms of the vertically integrated deviatoric stress tensor (Schoof, 2006b)

$$T_{ij} \approx \int dz \tau_{ij} = \int dz \left(2\nu\dot{\epsilon}_{ij}\right) \tag{18}$$

with $\tau_{ij}=\sigma_{ij}+p\delta_{ij}$, where the pressure $p$ is the isotropic part of the full stress tensor. Neglecting air pressure and assuming cryostatic pressure in the ice we get

$$T_{ij}n_j = \frac{1}{2}\left(1-\frac{\rho_\mathrm{i}}{\rho_\mathrm{o}}\right)\rho_\mathrm{i} g H_\mathrm{c}^2 n_i \, . \tag{19}$$





TCD
4, 1277–1306, 2010



In terms of SSA velocities $(v_x, v_y)$,

$$\bar{\nu} H_c \left\{ \left( 2\frac{\partial v_x}{\partial x} + \frac{\partial v_y}{\partial y} \right) n_x + \frac{1}{2} \left( \frac{\partial v_x}{\partial y} + \frac{\partial v_y}{\partial x} \right) n_y \right\} = \tau_{\text{stat}} n_x \,, \tag{20}$$

$$\bar{\nu} H_c \left\{ \left( \frac{\partial v_x}{\partial x} + 2\frac{\partial v_y}{\partial y} \right) n_y + \frac{1}{2} \left( \frac{\partial v_x}{\partial y} + \frac{\partial v_y}{\partial x} \right) n_x \right\} = \tau_{\text{stat}} n_y \,, \tag{21}$$

with $\boldsymbol{n}=(n_x, n_y)$ the horizontal, seaward-pointing vector normal to the calving front. The right-hand side of these equations, representing the static part of the stress balance $\tau_{\text{stat}}$, is computed according to the type of ice front concerned. In PISM-PIK, we distinguish between three types of ice-ocean interfaces, namely shelf calving fronts where

$$\tau_{\text{stat}} = \tau_{\text{stat}}^{\text{cf}} \equiv \frac{\rho_i g H_c^2}{4} \left( 1 - \frac{\rho_i}{\rho_o} \right) \,, \tag{22}$$

marine ice fronts (ice at the coast resting on bedrock below sea level) where

$$\tau_{\text{stat}} = \tau_{\text{stat}}^{\text{mf}} \equiv \frac{\rho_i g}{4} \left( H_c^2 - \frac{\rho_o}{\rho_i} (z_{\text{sl}} - b(x,y))^2 \right) \tag{23}$$

and cliffs (ice at the coast resting on bedrock above sea level) where

$$\tau_{\text{stat}} = \tau_{\text{stat}}^{\text{cl}} \equiv \frac{\rho_i g H_c^2}{4} \,. \tag{24}$$

These stress boundary conditions are applied directly at the calving front by replacing certain terms in the discretization of the SSA equations with the respective terms from the boundary condition. The implementation is described in detail in Appendix A.

Because of the dynamic calving law (Sect. 2.6 below), shelf tongues can break off the ice shelf and form (simulated) icebergs. These are identified and eliminated through a separate algorithm in PISM-PIK. This is necessary when using the boundary condition for the SSA equations because without a pinning point where ice is grounded these icebergs have zero total basal resistance in our model and therefore do not have unique velocities (cf. non-uniqueness up to "rigid body motions" in Schoof, 2006b).





TCD
4, 1277–1306, 2010



## 2.4 Continuous ice shelf advance and retreat through subgrid parametrization

In order to capture subgrid-scale advance and retreat of the calving front as depicted in Fig. 3 the mechanism introduced by Albrecht et al. (2010) is implemented in PISM-PIK. When an advancing ice shelf propagates into a new grid cell ($i+1$), this cell will be only partially-filled with respect to the horizontal area. The relevant field equations of Sect. 2.1 are not applied to partially-filled cells.

The subgrid parameterization is a precondition for the application of a continuous calving law because it models the observed almost vertical cliff-like shape of the calving fronts and preserves realistic driving stresses near the ice edge. In fact, without this mechanism artificially-thin ice shelf regions of only a few meters thickness may develop because in every timestep a small amount of ice is transported from the last shelf box into the next ice-free box.

A retreat of the calving front can be modeled in the same manner, i.e., by removing just the right amount of mass that accounts for a calving rate. (The calving rate itself is determined dynamically as described in Sect. 2.6.) That is, mass can be removed from partially filled cells at the ice front, and calving can advance into adjacent filled shelf cells, making them partially-filled.

## 2.5 Discretization scheme for mass transport

PISM uses a mass continuity scheme for SIA fluxes which has perfect numerical mass conservation (Bueler et al., 2005). The low-order mass continuity scheme used for SSA fluxes, as described in Bueler and Brown (2009), allows for local mass conservation errors. Keeping track of all mass fluxes and comparing their sum to the change in total ice volume has shown, that especially at ice margins problems arise.

We employ a modified scheme in PISM-PIK that is locally-mass conserving and that applies to both SIA and SSA velocities in the same way. Velocities are used on the same staggered grid: $\boldsymbol{v}_{\mathrm{SIA}}$ is already computed on the staggered grid, and $\boldsymbol{v}_{\mathrm{SSA}}$ is averaged onto it using adjacent regular grid values. The new scheme multiplies by the





TCD
4, 1277–1306, 2010



upwind ice thickness and applies a centered difference discretization:

$$\frac{\Delta H^i}{\Delta t} = -\frac{1}{\Delta x}\left[\begin{cases} v_x^{i+\frac{1}{2}} H^i, & v_x^{i+\frac{1}{2}} > 0 \\ v_x^{i+\frac{1}{2}} H^{i+1}, & v_x^{i+\frac{1}{2}} \le 0 \end{cases} - \begin{cases} v_x^{i-\frac{1}{2}} H^{i-1}, & v_x^{i-\frac{1}{2}} > 0 \\ v_x^{i-\frac{1}{2}} H^i, & v_x^{i-\frac{1}{2}} \le 0 \end{cases}\right]. \tag{25}$$

An analogous equation holds for the y-component. This scheme ensures mass conservation since every contribution of mass inflow in one box is necessarily a contribution to mass outflow in an adjacent box.

At the ice front the scheme needs to be slightly modified, since we do not compute velocities in ocean-boxes without ice. To avoid the zero velocity contribution of the ocean box adjacent to the last shelf box, when computing the staggered velocity at the calving front, we use the unstaggered SSA velocity from this last shelf box.

The properties of this alternative scheme for the pure-SIA mass continuity problem have been tested by comparison to the so-called Halfar similarity solution, and the results for the new scheme are as good as for the one from the PISM base version (Bueler et al., 2005). For the SSA it can be shown that the analytical solution from (Van der Veen, 1983) for an equilibrium ice shelf in the flow line case is better approximated using this alternative mass transport scheme (see also Albrecht et al., 2010). It is not necessary to modify the adaptive time-stepping from PISM base version to ensure the numerical stability of this scheme.

### 2.6 Calving law

Based on the observation by Doake et al. (1998) and Alley et al. (2008) that calving rate is linearly-related to the product of near-front thickness, half-width and strain rate, a local first-order law for large-scale ice shelf calving was introduced by Levermann et al. (2010) as a boundary condition to the mass continuity equation. This so-called Eigen Calving law has been implemented in PISM-PIK.

The applied calving rate is based on the eigenvalues $\dot{\epsilon}_\pm$ of the horizontal strain rate tensor (see Eq. 4). Along most areas of the calving front the corresponding





TCD
4, 1277–1306, 2010



eigen-directions will coincide with the directions parallel to and transverse to the flow (Fig. 4). In regions of divergent flow, where spreading occurs in both principle directions ($\dot{\epsilon}_{\pm}>0$), we define the rate of large-scale calving as

$$C = K \det(\dot{\boldsymbol{\epsilon}}) = K \dot{\epsilon}_{+} \dot{\epsilon}_{-} \quad \text{for} \quad \dot{\epsilon}_{\pm} > 0 \tag{26}$$

with $K>0$ being a proportionality constant.

Martin et al. (2010) show that this new dynamically motivated calving law enables PISM-PIK to reproduce realistic calving front positions for many of the ice shelves attached to the Antarctic ice sheet, across a broad range of ice thickness values.

## 3 MISMIP intercomparison

The numerical performance of PISM-PIK was tested in the context of the Marine Ice Sheet Model Intercomparison Project (MISMIP, Schoof et al., 2009). The results of these simulations allow a comparison with the semi-analytical solution by Schoof (2007a), and give insight into the quality of the numerical treatment of grounding line motion. The implementation of the calving front stress boundary condition (see Sect. 2.3) in PISM-PIK distinctly improves the performance compared to PISM, which used a notional shelf extension in ice-free ocean.

We consider only the MISMIP flow-line experiments on a constant slope bed (experiments 1 and 2) in this paper. As PISM-PIK is a three-dimensional model, a flow-line was simulated using periodic boundary conditions in the cross-flow direction. Calving occurs at a predetermined position in MISMIP and the calving law in Sect. 2.6 was not used. The model was run at resolutions of 12 km, 6 m and 3 km. Upon changes in flow parameter $A$ (Eq. 4), the position of grounding line should closely follow the semi-analytical solution, depicted as a solid black line in Fig. 5a. In order to diagnose the position of the grounding line at subgrid scale, a refinement based on Pattyn et al. (2006) was introduced in PISM-PIK. This subgrid treatment of the grounding line is





TCD
4, 1277–1306, 2010



only diagnostic in the MISMIP intercomparison description but it also provides a linear interpolation for bottom friction.

During experiment 1 the softness parameter $A$ is lowered stepwise. During experiment 2 these changes are reversed. Figure 5a shows the modeled grounding line position. It can be seen that (i) the movement of the grounding line is modelled qualitatively correctly at all resolutions, (ii) an offset from the semi-analytical solution is observed in experiment 1, and (iii) the offset is smaller in experiment 2. The offset in experiment 1 decreases with increasing resolution, while in experiment 2 it is independent of the resolution. The dependence on the resolution becomes evident in Fig. 6 which shows the steady-state grounding-line position of experiment 1 for various resolutions. The simulated grounding line positions converge to the semi-analytical solution upon grid-refinement.

For a flow-line setup governed by the SSA as considered here, the existence and properties of a shelf do not influence the grounding-line movement in the continuum model (Schoof, 2007a). In the implementation of the problem in PISM-PIK, however, we observe some (numerical) influence of the calving-front treatment on the steady-state results at low resolutions because the SSA stress balance equations are solved simultaneously for the entire computational domain encompassing sheet and shelf. The subgrid interpolation of the calving front as described in Sect. 2.4 ensures a controlled shelf growth, while without this treatment a very thin shelf develops immediately. Figure 6 shows that grounding line position performance with a subgrid treatment of the calving front is generally better than without, especially at low resolutions.

## 4 Conclusions

The large-scale marine ice sheet model PISM-PIK presented in this paper is based on the Parallel Ice Sheet Model (PISM), with major modifications for ice shelf and grounding line dynamics. A boundary condition for the SSA equations capturing the stress imbalance at the ice front was incorporated and a novel subgrid scheme for





TCD
4, 1277–1306, 2010



the advance and retreat of the calving front was introduced. This was combined with a physical dynamic calving law which is universal in the sense that it governs the calving process for different shelf geometries.

Grounded ice flow is captured as a direct superposition of velocities from two shallow approximations, SIA and SSA, a modification of the Bueler and Brown (2009) scheme. Both shallow approximations are solved simultaneously in the whole ice area. The new hybrid scheme allows for the treatment of all flow regimes in a consistent manner and permits a diagnostic definition of ice streams. It has been shown to provide a valid shallow approximation of the transition zone between ice sheet and ice shelf (Schoof and Hindmarsh, 2010). PISM-PIK thus includes a treatment of the transition from vertical-shearing dominated flow, in areas where the ice is frozen to the bed, to plug flow in ice shelves, which governs the ice flux across the grounding line.

As a first application, the performance of PISM-PIK was tested in context of the Marine Ice Sheet Model Intercomparison Project. In these experiments, the model reproduced the semi-analytically predicted grounding line position dependence on ice softness for the flow-line case, with convergence towards the semi-analytical solution with grid refinement.

The second part of this paper presents a dynamic equilibrium simulation for Antarctica (Martin et al., 2010), demonstrating the ability of PISM-PIK to simulate whole sheet-shelf systems.

## Appendix A

### On the discretization of the calving front stress boundary condition

In the following we detail the implementation of the calving front boundary condition into the SSA-scheme. We only describe the scheme for SSA equation (7). The second





TCD
4, 1277–1306, 2010



equation based on (8) is similar. Discretizing the outer derivatives of Eq. (7) yields

$$\frac{2}{\Delta x}(\bar{\nu}H)\Big|_{i+\frac{1}{2}}^{j}\left(2\frac{\partial v_x}{\partial x}+\frac{\partial v_y}{\partial y}\right)\Bigg|_{i+\frac{1}{2}}^{j}-\frac{2}{\Delta x}(\bar{\nu}H)\Big|_{i-\frac{1}{2}}^{j}\left(2\frac{\partial v_x}{\partial x}+\frac{\partial v_y}{\partial y}\right)\Bigg|_{i-\frac{1}{2}}^{j}$$
$$+\frac{1}{\Delta y}(\bar{\nu}H)\Big|_{i}^{j+\frac{1}{2}}\left(\frac{\partial v_x}{\partial y}+\frac{\partial v_y}{\partial x}\right)\Bigg|_{i}^{j+\frac{1}{2}}-\frac{1}{\Delta y}(\bar{\nu}H)\Big|_{i}^{j-\frac{1}{2}}\left(\frac{\partial v_x}{\partial y}+\frac{\partial v_y}{\partial x}\right)\Bigg|_{i}^{j-\frac{1}{2}}$$
$$=\rho_{\mathrm{i}}gH\frac{\partial h}{\partial x}.$$

The next step is to replace the four expressions of the form $\left(2\frac{\partial v_{\{ij\}}}{\partial\{ij\}}+\frac{\partial v_{\{ij\}}}{\partial\{ij\}}\right)$ with the respective terms from the boundary condition (20). Using the boundary-indicators $a_{\pm}, b_{\pm}$ (see Fig. 7) leads to

$$a_{+}\frac{2}{\Delta x}(\bar{\nu}H)\Big|_{i+\frac{1}{2}}^{j}\left(2\frac{\partial v_x}{\partial x}+\frac{\partial v_y}{\partial y}\right)\Bigg|_{i+\frac{1}{2}}^{j}-a_{-}\frac{2}{\Delta x}(\bar{\nu}H)\Big|_{i-\frac{1}{2}}^{j}\left(2\frac{\partial v_x}{\partial x}+\frac{\partial v_y}{\partial y}\right)\Bigg|_{i-\frac{1}{2}}^{j}$$
$$+b_{+}\frac{1}{\Delta y}(\bar{\nu}H)\Big|_{i}^{j+\frac{1}{2}}\left(\frac{\partial v_x}{\partial y}+\frac{\partial v_y}{\partial x}\right)\Bigg|_{i}^{j+\frac{1}{2}}-b_{-}\frac{1}{\Delta y}(\bar{\nu}H)\Big|_{i}^{j-\frac{1}{2}}\left(\frac{\partial v_x}{\partial y}+\frac{\partial v_y}{\partial x}\right)\Bigg|_{i}^{j-\frac{1}{2}}$$
$$=\rho_{\mathrm{i}}gH\frac{\partial h}{\partial x}+\left(a_{+}-a_{-}\right)\frac{2}{\Delta x}\tau_{\mathrm{stat}},$$

where $a_{\pm}, b_{\pm}$=0 if one or both of the adjacent cells are ice-free, and $a_{\pm}, b_{\pm}$=1 otherwise, and where the value of $\tau_{\mathrm{stat}}$ is determined by one of Eqs. (22), (23) or (24). The calving front is situated at the border between ocean cells and the last completely-filled shelf cells; the stress boundary condition is not applied to partially-filled cells that arise due to the subgrid parameterization described in Sect. 2.4.

Further discretization yields:

$$a_{+}\frac{4}{\Delta x}(\bar{\nu}H)\Big|_{i+\frac{1}{2}}^{j}\left[\frac{\partial v_x}{\partial x}\Bigg|_{i+\frac{1}{2}}^{j}\right.$$





TCD
4, 1277–1306, 2010



$$
\begin{aligned}
&+\frac{1}{8}\left(b_{+E}\frac{\partial v_y}{\partial y}\Big|_{i+1}^{j+\frac{1}{2}}+b_{-E}\frac{\partial v_y}{\partial y}\Big|_{i+1}^{j-\frac{1}{2}}+b_{+}\frac{\partial v_y}{\partial y}\Big|_{i}^{j+\frac{1}{2}}+b_{-}\frac{\partial v_y}{\partial y}\Big|_{i}^{j-\frac{1}{2}}\right)\Bigg]\\
&-a_{-}\frac{4}{\Delta x}(\bar{\nu}H)\Big|_{i-\frac{1}{2}}^{j}\Bigg[\frac{\partial v_x}{\partial x}\Big|_{i-\frac{1}{2}}^{j}\\
&+\frac{1}{8}\left(b_{+}\frac{\partial v_y}{\partial y}\Big|_{i}^{j+\frac{1}{2}}+b_{-}\frac{\partial v_y}{\partial y}\Big|_{i}^{j-\frac{1}{2}}+b_{+W}\frac{\partial v_y}{\partial y}\Big|_{i-1}^{j+\frac{1}{2}}+b_{-W}\frac{\partial v_y}{\partial y}\Big|_{i-1}^{j-\frac{1}{2}}\right)\Bigg]\\
&+b_{+}\frac{1}{\Delta y}(\bar{\nu}H)\Big|_{i}^{j+\frac{1}{2}}\Bigg[\frac{\partial v_x}{\partial y}\Big|_{i}^{j+\frac{1}{2}}\\
&+\frac{1}{4}\left(a_{+N}\frac{\partial v_y}{\partial x}\Big|_{i+\frac{1}{2}}^{j+1}+a_{+}\frac{\partial v_y}{\partial x}\Big|_{i+\frac{1}{2}}^{j}+a_{-N}\frac{\partial v_y}{\partial x}\Big|_{i-\frac{1}{2}}^{j+1}+a_{-}\frac{\partial v_y}{\partial x}\Big|_{i-\frac{1}{2}}^{j}\right)\Bigg]\\
&-b_{-}\frac{1}{\Delta y}(\bar{\nu}H)\Big|_{i}^{j-\frac{1}{2}}\Bigg[\frac{\partial v_x}{\partial y}\Big|_{i}^{j-\frac{1}{2}}\\
&+\frac{1}{4}\left(a_{+}\frac{\partial v_y}{\partial x}\Big|_{i+\frac{1}{2}}^{j}+a_{+S}\frac{\partial v_y}{\partial x}\Big|_{i+\frac{1}{2}}^{j-1}+a_{-}\frac{\partial v_y}{\partial x}\Big|_{i-\frac{1}{2}}^{j}+a_{-S}\frac{\partial v_y}{\partial x}\Big|_{i-\frac{1}{2}}^{j-1}\right)\Bigg]\\
&=\rho_{\mathrm{i}}gH\Big|_{i}^{j}\frac{\partial h}{\partial x}+(a_{+}-a_{-})\frac{2}{\Delta x}\tau_{\mathrm{stat}}\Big|_{i}^{j}\,.
\end{aligned}
$$

The fact that we do not modify the structure of the discretization at the calving front partially neglects the derivatives of $v_y$ in Eq. (7) (and of $v_x$ in Eq. 8) depending on the value of the boundary indicators for each specific calving front shape.





TCD
4, 1277–1306, 2010



*Acknowledgements.* M. Haseloff and T. Albrecht were funded by the German National Academic Foundation; M. A. Martin and R. Winkelmann by the TIPI project of the WGL. E. Bueler and C. Khroulev are supported by NASA grant NNX09AJ38G. We thank Jed Brown (ETH Zurich, Switzerland) for advice on PISM, and Florian Ziemen (MPI Hamburg, Germany) for fruitful discussions and his idea for the mass transport scheme.

## References

Albrecht, T., Martin, M. A., Winkelmann, R., Haseloff, M., and Levermann, A.: Parametrization for subgrid-scale motion of ice-shelf calving-fronts, The Cryosphere Discuss., submitted, 2010. 1278, 1288, 1289

Alley, R. B., Horgan, H. J., Joughin, I., Cuffey, K. M., Dupont, T. K., Parizek, B. R., Anandakrishnan, S., and Bassis, J.: A simple law for ice-shelf calving, Science, 322, p. 1344, 2008. 1289

Bamber, J. L., Alley, R. B., and Joughin, I.: Rapid response of modern day ice sheets to external forcing, Earth Planet. Sc. Lett., 257, 1–13, 2007. 1280

Blatter, H.: Velocity and stress fields in grounded glaciers: a simple algorithm for including deviatoric stress gradients, J. Glaciol., 41, 333–344, 1995. 1279

Bueler, E. and Brown, J.: The shallow shelf approximation as a sliding law in a thermomechanically coupled ice sheet model, J. Geophys. Res., 114, F03008, doi:10.1029/2008JF001179, 2009. 1278, 1280, 1281, 1282, 1284, 1285, 1286, 1288, 1292

Bueler, E., Khroulev, C., Aschwanden, A.: Parallel Ice Sheet Model – open source website, 2008. 1281

Bueler, E., Lingle, C., Kallen-Brown, J., Covey, D., and Bowman, L.: Exact solutions and verification of numerical models for isothermal ice sheets, J. Glaciol., 51, 291–306, 2005. 1288, 1289

Bueler, E., Brown, J., and Lingle, C.: Exact solutions to the thermomechanically coupled shallow-ice approximation: effective tools for verification, J. Glaciol., 53, 499–516, 2007. 1281

De Angelis, H. and Skvarca, P.: Glacier surge after ice shelf collapse, Science, 299, 1560–1563, 2003. 1280





TCD

4, 1277–1306, 2010



Doake, C. S. M., Corr, H. F. J., Skvarca, P., and Young, N. W.: Breakup and conditions for stability of the Northern Larsen ice shelf, Antarctica, Nature, 391, 778–780, 1998. 1289
Dupont, T. K. and Alley, R. B.: Assessment of the importance of ice-shelf buttressing to ice-sheet flow, Geophys. Res. Lett., 32, L04503, doi:10.1029/2004GL022024, 2005. 1278
Fowler, A. C.: Modelling the Flow of Glaciers and Ice Sheets, Continuum Mechanics and Applications in Geophysics and the Environment, Springer, 201–221, 2001. 1285
Glasser, N. F. and Scambos, T. A.: A structural glaciological analysis of the 2002 Larsen B ice shelf collapse, J. Glaciol., 54, 3–16, 2008. 1280
Goldberg, D., Holland, D. M., and Schoof, C.: Grounding line movement and ice shelf buttressing in marine ice sheets, J. Geophys. Res., 114, F04026, doi:10.1029/2008JF001227, 2009. 1280
Greve, R.: Application of a polythermal three-dimensional ice sheet model to the Greenland ice sheet: response to steady-state and transient climate scenarios, J. Climate, 10, 901–918, 1997b. 1279
Greve, R. and Blatter, H. (Eds.): Dynamics of Ice Sheets and Glaciers, Springer, 2009. 1282
Hutter, K. (Ed.): Theoretical Glaciology, D. Reidel Publishing Company/Terra Scientific Publishing Company, 1983. 1279, 1283
Huybrechts, P.: A 3-D model for the Antarctic ice-sheet: a sensitivity study on the glacial-interglacial contrast, Clim. Dynam., 5, 79–92, 1990. 1279
Jarosch, A. H. and Gudmundsson, M. T.: Numerical studies of ice flow over subglacial geothermal heat sources at Grímsvötn, Iceland, using Full Stokes equations, J. Geophys. Res., 112, F02008, doi:10.1029/2006JF000540, 2007. 1279
Le Brocq, A. M., Payne, A. J., and Vieli, A.: Antarctic dataset in netCDF format, doi:10.1594/PANGAEA.734145, available at: http://doi.pangaea.de/10.1594/PANGAEA.734145, 2010. 1281
Levermann, A., Albrecht, T., Winkelmann, R., Martin, M. A., and Haseloff, M.: Universal dynamic calving law implies potential for abrupt ice-shelf retreat, submitted, 2010. 1289
Lythe, M. B., Vaughan, D. G., and BEDMAP Consortium: BEDMAP: A new ice thickness and subglacial topographic model of Antarctica, J. Geophys. Res., 106, 11335–11351, 2001. 1281
MacAyeal, D. R.: Large-scale ice flow over a viscous basal sediment – Theory and application to ice stream B, Antarctica, J. Geophys. Res., 94, 4071–4087, 1989. 1284
MacAyeal, D. R., Rommelaere, V., Huybrechts, P., Hulbe, C. L., Determann, J., and Ritz, C.:





TCD
4, 1277–1306, 2010



An ice-shelf model test based on the Ross Ice Shelf, Ann. Glaciol., 23, 46–51, 1996. 1279, 1286
Marshall, S. J., Tarasov, L., Clarke, G. K. C., and Peltier, W. R.: Glaciological reconstruction of the Laurentide Ice Sheet: physical processes and modelling challenges, Canad. J. Earth Sci., 37, 769–793, 2000. 1279
Martín, C., Navarro, F., Otero, J., Cuadrado, M. L., and Corcuera, M. I.: Three-dimensional modelling of the dynamics of Johnsons Glacier, Livingston Island, Antarctica, Ann. Glaciol., 39, 1–8, 2004. 1279
Martin, M. A., Winkelmann, R., Haseloff, M., Albrecht, T., Bueler, E., Khroulev, C., and Levermann, A.: The Potsdam Parallel Ice Sheet Model (PISM-PIK) – Part 2: Dynamic equilibrium simulation of the Antarctic ice sheet, The Cryosphere Discuss., 4, 1307-1341, doi:10.5194/tcd-4-1307-2010, 2010. 1278, 1280, 1281, 1290, 1292
Morland, L. W.: Unconfined ice-shelf flow, in: Dynamics of the West Antarctic ice sheet, edited by: der Veen, C. J. V. and Oerlemans, J., Cambridge University Press, Cambridge, UK and New York, NY, USA, 1987. 1279, 1283
Morland, L. W. and Johnson, I. R.: Steady motion of ice sheets, J. Glaciol., 25, 229–246, 1980. 1283
Morland, L. W. and Zainuddin, R.: Plane and radial ice-shelf flow with prescribed temperature profile, in: Dynamics of the West Antarctic Ice Sheet, edited by: Van der Veen, C. J. and Oerlemans, J., Reidel Publ., Dordrecht, the Netherlands, 99–116, 1987. 1286
Paterson, W.: The Physics of Glaciers, Elsevier, Oxford, 1994. 1284
Paterson, W. S. B. and Budd, W. F.: Flow parameters for ice sheet modelling, Cold. Reg. Sci. Technol., 6, 175–177, 1982. 1282
Pattyn, F.: A new three-dimensional higher-order thermomechanical ice sheet model: Basic sensitivity, ice stream development, and ice flow across subglacial lakes, J. Geophys. Res., 108, 2382–2397, 2003. 1279
Pattyn, F.: Investigating the stability of subglacial lakes with a full Stokes ice sheet model, J. Glaciol.,54, 353–361, 2008. 1279
Pattyn, F., Huyghe, A., De Brabander, S., and De Smedt, B.: Role of transition zones in marine ice sheet dynamics, J. Geophys. Res., 111, 2004–2014, 2006. 1290
Payne, A. J.: A thermomechanical model of ice flow in West Antarctica, Clim. Dynam., 15, 115–125, 1999. 1279
Pollard, D. and Deconto, R. M.: Modelling West Antarctic ice sheet growth and collapse through





TCD
4, 1277–1306, 2010



the past five million years, Nature, 458, 329–332, 2009. 1279
Rignot, E., Bamber, J. L., den Broeke, M. R. V., Li, Y., Davis, C., de Berg, W. J. V., and Meijgaard, E.: Recent Antarctic ice mass loss from radar interferometry and regional climate modelling, Nat. Geosci., 1, 106–110, 2008. 1280
Ritz, C., Rommelaere, V., and Dumas, C.: Modeling the evolution of Antarctic ice sheet over the last 420 000 years: Implications for altitude changes in the Vostok region, J. Geophys. Res., 106, 31943–31964, 2001. 1279
Rott, H., Rack, W., and Nagler, T.: Increased export of grounded ice after the collapse of northern Larsen ice shelf, Antarctic Peninsula, observed by Envisat ASAR, Geoscience and Remote Sensing Symposium, IEEE International, 1174–1176, 2007. 1280
Schoof, C.: Variational methods for glacier flow over plastic till, J. Fluid Mech., 555, 299–320, 2006a. 1280, 1284
Schoof, C.: A variational approach to ice stream flow, J. Fluid Mech., 556, 227–251, 2006b. 1283, 1286, 1287
Schoof, C.: Marine ice-sheet dynamics. Part 1. The case of rapid sliding, J. Fluid Mech., 573, 27–55, 2007a. 1290, 1291
Schoof, C.: Ice sheet grounding line dynamics: Steady states, stability, and hysteresis, J. Geophys. Res., 112, F03S28, doi:10.1029/2006JF000664, 2007b. 1279
Schoof, C. and Hindmarsh, R. C. A.: Thin-film flows with wall slip: An asymptotic analysis of higher order glacier flow models, Q. J. Mech. Appl. Math., 63, 73-114, doi:10.1093/qjmam/hbp025, 2010. 1285, 1292
Schoof, C., Hindmarsh, R. C. A., and Pattyn, F.: MISMIP: Marine ice sheet model intercomparison project, available at: http://homepages.ulb.ac.be/~fpattyn/mismip/, 2009. 1290
Van der Veen, C. J.: A note on the equilibrium porfile of a free floating ice shelf, IMAU Report V83-15. State University Utrecht, 1983. 1289
Weertman, J.: Deformation of floating ice shelves, J. Glaciol., 3, 38–42, 1957. 1286
Weis, M., Greve, R., and Hutter, K.: Theory of shallow ice shelves, Continuum Mech. Therm., 11, 15–50, 1999. 1279, 1283





TCD
4, 1277–1306, 2010



**Table 1.** Table of symbols.

| Symbol | Description | SI units |
|---|---|---|
| $A(T^*)$ | ice softness | $\mathrm{Pa}^{-3}\,\mathrm{s}^{-1}$ |
| $B(T^*)$ | ice hardness; $B(T^*)=A(T^*)^{-\frac{1}{n}}$ | $\mathrm{Pa}\,\mathrm{s}^{1/3}$ |
| $\bar{B}$ | vertically averaged ice hardness $\bar{B}=H^{-1}\int_b^h B(T^*)dz$ | $\mathrm{Pa}\,\mathrm{s}^{1/3}$ |
| $b$ | bedrock elevation | m |
| $C$ | calving rate | $\mathrm{m}\,\mathrm{s}^{-1}$ |
| $c_\mathrm{i}$ | specific heat capacity for ice | $\mathrm{J}\,(\mathrm{kg}\,\mathrm{K})^{-1}$ |
| $E_\mathrm{SIA}$ | enhancement factor for the SIA | |
| $E_\mathrm{SSA}$ | enhancement factor for the SSA | |
| $g$ | acceleration due to gravity | $\mathrm{m}\,\mathrm{s}^{-2}$ |
| $h$ | upper surface elevation of ice | m |
| $H$ | ice thickness | m |
| $H_c$ | ice thickness at calving front | m |
| $\{i,j\}$ | 2-D horizontal tensor indices | |
| $K$ | proportionality constant for Eigen Calving | m s |
| $k_\mathrm{i}$ | thermal conductivity of ice | $\mathrm{W}\,(\mathrm{K}\,\mathrm{m})^{-1}$ |
| $M$ | ice equivalent surface mass balance | $\mathrm{m}\,\mathrm{s}^{-1}$ |
| $n$ | Glen flow law exponent | |
| $n_i$ | component $i$ of the seaward pointing normal vector at calving front | |
| $p$ | pressure=isotropic part of full stress tensor: $p=1/3\,\sigma_{kk}$ | $\mathrm{Pa}=\mathrm{N}\,\mathrm{m}^{-2}$ |
| $p_\mathrm{w}$ | pore water pressure | $\mathrm{N}\,\mathrm{m}^{-2}$ |
| $\boldsymbol{Q}$ | horizontal ice flux | $\mathrm{m}^2\,\mathrm{s}^{-1}$ |
| $S$ | ice equivalent basal mass balance ($S>0$ is melting) | $\mathrm{m}\,\mathrm{s}^{-1}$ |
| $T$ | ice temperature | K |
| $T^*$ | pressure-adjusted temperature | K |
| $T_{ij}$ | vertically integrated deviatoric stress tensor | $\mathrm{Pa}\,\mathrm{m}=\mathrm{N}\,\mathrm{m}^{-1}$ |
| $\boldsymbol{v}$ | overall horizontal ice velocity | $\mathrm{m}\,\mathrm{s}^{-1}$ |
| $\boldsymbol{v}_\mathrm{b}$ | basal ice velocity; $\boldsymbol{v}_\mathrm{b}=\boldsymbol{v}_\mathrm{SSA}=(v_x,v_y)$ | $\mathrm{m}\,\mathrm{s}^{-1}$ |
| $\boldsymbol{v}_\mathrm{SIA}$ | SIA velocity of ice | $\mathrm{m}\,\mathrm{s}^{-1}$ |
| $\boldsymbol{v}_\mathrm{SSA}$ | SSA velocity of ice; $\boldsymbol{v}_\mathrm{SSA}=(v_x,v_y)$ | $\mathrm{m}\,\mathrm{s}^{-1}$ |
| $(x,y)$ | horizontal dimensions | m |
| $z$ | vertical dimension (positive upwards) | m |
| $z_\mathrm{sl}$ | sea level | m |
| $\delta_{ij}$ | Kronecker delta | |
| $\Delta x,\Delta y$ | horizontal grid size | km |
| $\boldsymbol{\nabla}$ | 2 dimensional nabla operator $\boldsymbol{\nabla}=(\partial_x,\partial_y)$ | $\mathrm{m}^{-1}$ |
| $\dot{\epsilon}_{ij}$ | strain rate tensor | $\mathrm{s}^{-1}$ |
| $\dot{\epsilon}_\pm$ | eigenvalues of strain rate tensor | $\mathrm{s}^{-1}$ |
| $\{\mu,\nu\}$ | 3-D tensor indices | |
| $\nu$ | viscosity $\nu=1/2\,B(T^*)^{(1-n)/n}$ | Pa s |
| $\tilde{\nu}$ | effective viscosity | Pa s |
| $\rho_\mathrm{i}$ | density of ice | $\mathrm{kg}\,\mathrm{m}^{-3}$ |
| $\rho_\mathrm{o}$ | density of ocean water | $\mathrm{kg}\,\mathrm{m}^{-3}$ |
| $\sigma_{ij}$ | full Cauchy stress tensor; $\sigma_{ij}=\tau_{ij}-p\delta_{ij}$ | $\mathrm{Pa}=\mathrm{N}\,\mathrm{m}^{-2}$ |
| $\tau_\mathrm{b}$ | basal shear stress on ice | $\mathrm{Pa}=\mathrm{N}\,\mathrm{m}^{-2}$ |
| $\tau_\mathrm{c}$ | yield stress | $\mathrm{Pa}=\mathrm{N}\,\mathrm{m}^{-2}$ |
| $\tau_{ij}$ | deviatoric stress tensor; $\tau_{ij}=2\nu\dot{\epsilon}_{ij}$ | $\mathrm{Pa}=\mathrm{N}\,\mathrm{m}^{-2}$ |
| $\tau_\mathrm{stat}$ | vertically integrated static stress at calving front | $\mathrm{Pa}\,\mathrm{m}=\mathrm{N}\,\mathrm{m}^{-1}$ |
| $\phi$ | till friction angle | ° |





TCD
4, 1277–1306, 2010



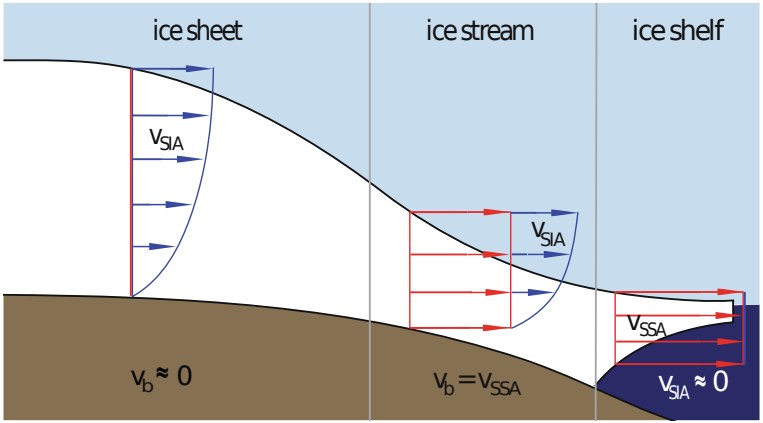


**Fig. 1.** Schematic diagram of ice profile and different flow regimes. Throughout the grounded ice region, the ice velocity is determined by linear superposition of the SIA and the SSA velocities. *Ice sheet* with negligible basal sliding. The velocity is dominated by the Shallow Ice Approximation. Friction at the bed leads to shearing in the ice column and a velocity profile depicted in blue. *Ice stream*. Both SIA and SSA velocities are relevant for the ice flow. SSA serves as a sliding law for the shear flow. *Ice shelf*. The plug flow regime is dominated by the Shallow Shelf Approximation leading to a uniform vertical velocity profile.





TCD
4, 1277–1306, 2010



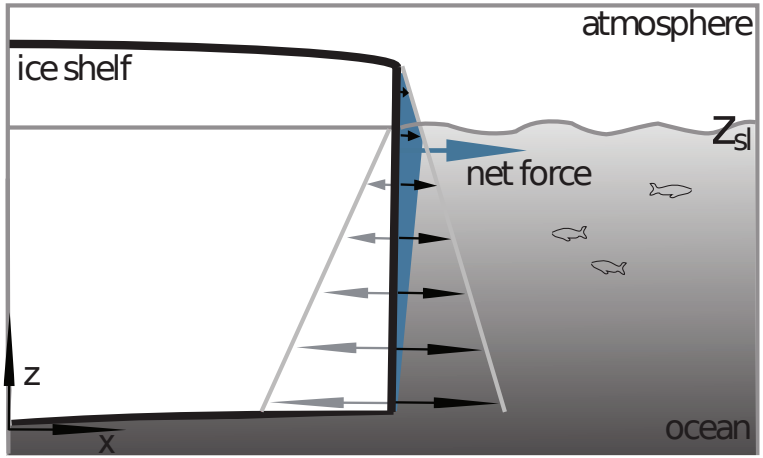


**Fig. 2.** Schematic diagram of forces at the calving front. Hydrostatic pressure (grey) and cryostatic pressure (black) result in net force in direction of the ocean (blue). The net force is significantly reduced compared to a situation where the hydrostatic pressure is neglected.





TCD
4, 1277–1306, 2010



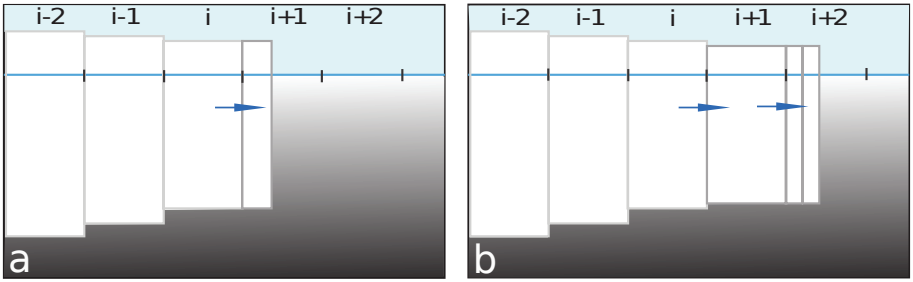


**Fig. 3.** Schematic diagram illustrating subgrid-scale advance of the calving front. As a new grid cell $i+1$ is partially filled with ice its ice thickness is kept constant at the same value as grid cell $i$.





TCD
4, 1277–1306, 2010



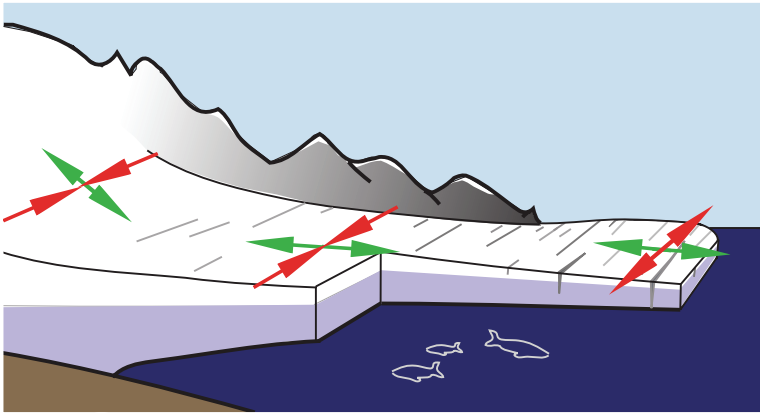

**Fig. 4.** Schematic diagram of dynamic calving law (see Eq. 26). Green arrows denote the eigen-direction along the flow direction, red arrows the eigen-direction perpendicular to the flow direction. Convergence of ice flow perpendicular to the main flow direction is associated with closure of crevasses whereas spreading in both directions (corresponding to positive eigenvalues $\dot{\epsilon}_{\pm}$) is associated with intersecting crevasses and enhanced calving.





TCD
4, 1277–1306, 2010



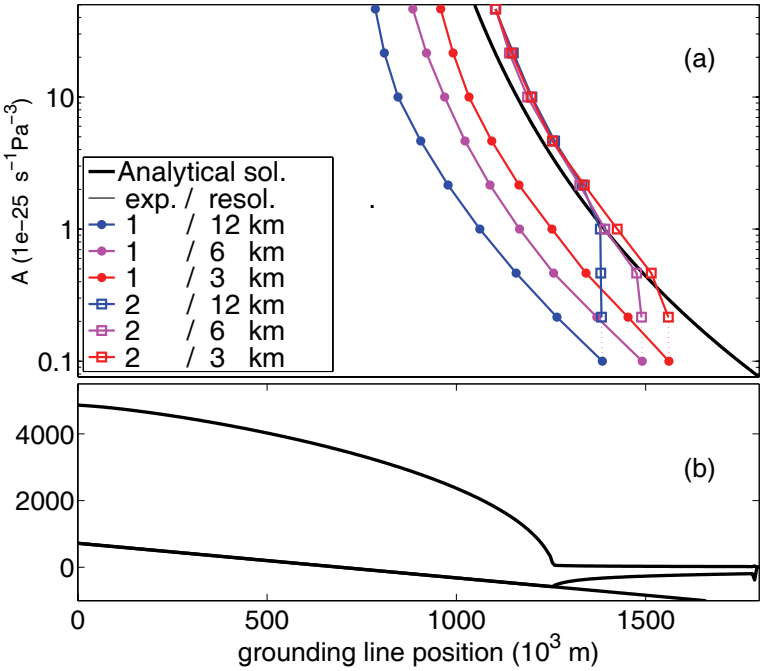


**Fig. 5.** MISMIP experiments on a constant slope bed. **(a)** Dependence of grounding-line position on rate factor $A$. Solid black line: semi-analytical prediction. Colored lines: simulation results with PISM-PIK, at $\Delta x$=12, 6, 3 km resolution. **(b)** Example ice sheet profile.





TCD
4, 1277–1306, 2010



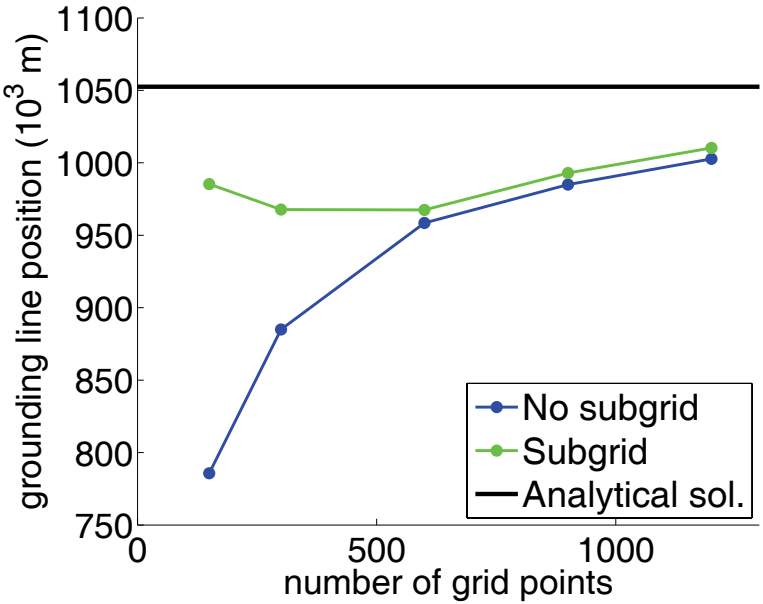


**Fig. 6.** Grounding-line position vs. resolution for experiment 1, step 1 of MISMIP. Green: with sub-grid treatment of the calving front motion, blue: without. Black line: semi-analytical prediction.





TCD
4, 1277–1306, 2010



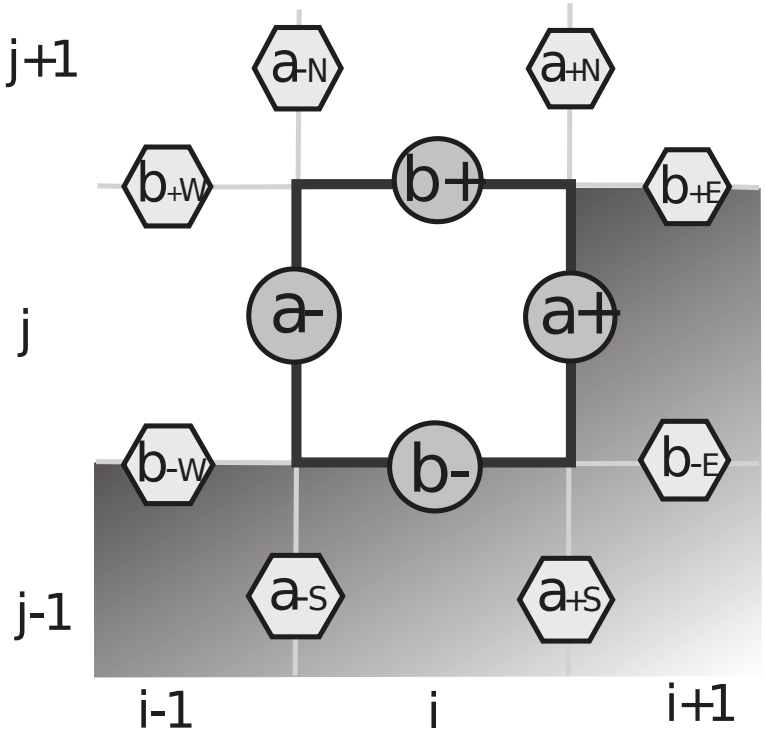


**Fig. 7.** Stencil for the SSA boundary condition in the case of an ice-filled (white) cell with ice-filled and ice-free (shaded) neighbors. For this specific shape of the calving front the boundary indicators $a_-, b_+$ and $a_{-N}, a_{+N}, b_{+W}$ have the value 1, whereas $a_+, b_-$ and $a_{-S}$, $a_{+S}, b_{-W}, b_{-E}, b_{+E}$ have value 0.





TCD
4, 1277–1306, 2010